Check for updates

AGU ADVANCING EARTH AND SPACE SCIENCES

JGR Planets

RESEARCH ARTICLE
10.1029/2025JE009008

Enceladus Water Plume Modeling Using DSMC

A. Mahieux[1,2,3], D. B. Goldstein[1], P. L. Varghese[1], L. M. Trafton[4], G. Portyankina[5], L. W. Esposito[6], M. E. Perry[7], J. H. Waite[8], B. S. Southworth[9], and S. Kempf[6]

[1]Department of Aerospace Engineering and Engineering Mechanics, The University of Texas at Austin, Austin, TX, USA, [2]Belgian Institute for Space Aeronomy, Brussels, Belgium, [3]Aurora Technology service for the European Space Agency, Madrid, Spain, [4]The University of Texas at Austin, McDonald Observatory, Austin, TX, USA, [5]Standort Berlin Deutschen Zentrums für Luft- und Raumfahrt (DLR), Berlin, Germany, [6]Laboratory for Atmospheric and Space Physics, University of Colorado Boulder, Boulder, CO, USA, [7]Johns Hopkins University Applied Physics Laboratory, Laurel, MD, USA, [8]Department of Physics and Astronomy, The University of Alabama, Tuscaloosa, AL, USA, [9]Los Alamos National Laboratory, Los Alamos, NM, USA

Key Points:

- Updated values for the total mass flow rate outgassed from the Tiger Stripes using comprehensive Direct Simulation Monte Carlo simulations
- New constraints on the ice grain radii and vent exit temperatures
- Method to reduce the size of an under constrained problem

Supporting Information:

Supporting Information may be found in the online version of this article.

Correspondence to:

A. Mahieux,
arnaud.mahieux@utexas.edu

Citation:

Mahieux, A., Goldstein, D. B., Varghese, P. L., Trafton, L. M., Portyankina, G., Esposito, L. W., et al. (2025). Enceladus water plume modeling using DSMC. *Journal of Geophysical Research: Planets*, *130*, e2025JE009008. https://doi.org/10.1029/2025JE009008

Received 21 FEB 2025
Accepted 14 AUG 2025

Author Contributions:

Conceptualization: A. Mahieux
Data curation: G. Portyankina, L. W. Esposito, M. E. Perry, J. H. Waite, B. S. Southworth, S. Kempf
Funding acquisition: D. B. Goldstein, P. L. Varghese, L. M. Trafton
Methodology: A. Mahieux, D. B. Goldstein, P. L. Varghese, L. M. Trafton
Project administration: D. B. Goldstein, P. L. Varghese
Resources: D. B. Goldstein, P. L. Varghese
Software: A. Mahieux
Supervision: D. B. Goldstein, L. M. Trafton
Validation: A. Mahieux
Writing – original draft: A. Mahieux

© 2025. The Author(s).
This is an open access article under the terms of the Creative Commons Attribution-NonCommercial-NoDerivs License, which permits use and distribution in any medium, provided the original work is properly cited, the use is non-commercial and no modifications or adaptations are made.

Abstract This study investigates the water plumes of Saturn's moon, Enceladus, using Direct Simulation Monte Carlo (DSMC) modeling to analyze venting dynamics and plume structures. Building on prior research, we employ a parametrized DSMC approach to model water vapor and ice particle flows, leveraging Cassini spacecraft data from instruments such as the Ion and Neutral Mass Spectrometer and the Ultraviolet Imaging Spectrograph. The study explores whether vent conditions, such as mass flow rates, mixture temperatures, and particle sizes, can be inferred from observational data. We develop a computational framework to expand plume simulations beyond 10 km altitudes, incorporating gravitational and inertial forces in an Enceladus-fixed reference frame. A sensitivity analysis correlates vent parameters with observed data, identifying critical contributors such as vent orientation and location, mass flow rate, exit temperature, and ice grain characteristics. This approach reduces the dimensionality of fitting procedures, enabling robust parameter constraints and a more detailed understanding of plume dynamics. Key findings include constrained values for mass flow rates, ice grain radii assuming single-size particles, and exit temperatures (~44–61 K), consistent with theoretical predictions. Additionally, variations in vent orientation and positional parameters were refined from the work of Porco et al. (2014, https://doi.org/10.1088/0004-6256/148/3/45). These results highlight the importance of collision dynamics in shaping plume structures. This work establishes a computationally efficient methodology for analyzing cryovolcanic plumes applicable to future missions exploring icy moons such as Enceladus or Europa. By prioritizing sensitive parameters, the study offers insights for optimizing observational strategies to maximize scientific yield.

Plain Language Summary This study examines the water plumes of Saturn's moon Enceladus using computer simulations to understand how water vapor and ice particles escape to space. Data from NASA's Cassini spacecraft are used together with the Direct Simulation Monte Carlo modeling technique to study the structure and behavior of these plumes. The study focuses on key factors such as the speed and temperature of the escaping material as well as the size of the ice grains—assuming single-size particles—to determine how well these could be inferred from Cassini's observations. By refining previous models, this work extends the simulations to altitudes beyond 10 km, considering the effects of gravity and motion on the plume. The findings provide new estimates for the amount of material ejected, ice grain sizes (~1.1 μm), and vent temperatures (~44–61 K), improving previous models. This study could help with future missions, such as those to Jupiter's moon Europa or ESA's L-class future mission to Enceladus, by identifying the most important parameters for studying cryovolcanic activity and optimizing spacecraft observations.

1. Introduction

The Enceladus geysers, located in its South Polar Region, were first reported in 2005 by Cassini. Various instruments onboard the spacecraft (Schenk et al., 2018; Science Special Issue, 2006) performed observations of the plumes, while many studies focused on their characterization, as they offer an unprecedented opportunity to study the interior of this icy moon of Saturn. Many studies have shown that the outgassed material is mainly composed of water vapor and water-ice particles, together with other trace gases such as nitrogen-bearing and oxygen-bearing, and aromatic compounds (Hansen et al., 2011; Khawaja et al., 2019; Magee & Waite, 2017; Postberg, Khawaja, et al., 2018; Waite et al., 2006, 2017).

Writing – review & editing:
D. B. Goldstein, P. L. Varghese,
L. M. Trafton, G. Portyankina,
L. W. Esposito, M. E. Perry, J. H. Waite,
B. S. Southworth, S. Kempf

The geysers originate from many tens-of-kilometer-long crevasses, named the Tiger Stripes, and the plumes extend far into space: the ice grains ultimately form the Saturn E-ring. Ground temperature in the Tiger Stripe region was measured by the Composite Infrared Spectrometer (CIRS) (Howett et al., 2011; Spencer et al., 2006) and showed that the crevasses in the South Polar region were dramatically warmer than the surrounding regions (∼135 K) and the rest of the satellite surface (<80 K). Using the Imaging Science Subsystem (ISS) imaging and triangulating the visible particulate streams, Porco et al. (2014) reported the location and orientation of 98 vents at the surface.

Several studies have focused on the origin of the geyser phenomena: near-surface explosive boiling liquid water (Porco et al., 2006), clathrate decomposition (Kieffer et al., 2006), and evaporation from an underground salty ocean (Porco et al., 2014; Postberg et al., 2009, 2011; Schmidt et al., 2008). Several authors studied the flow inside the vent using a gas dynamics model (Ingersoll & Pankine, 2010; Schmidt et al., 2008; Yeoh et al., 2015; Zaharias et al., 2023). Others focused on the formation of particles, which were explained to be the results of sprays from bursting bubbles, the latter stemming from rising exsolved gases such as CO_2 (Matson et al., 2018). Other studies have described how fluids move up the conduits (Ingersoll & Nakajima, 2016; Kite & Rubin, 2016; Nakajima & Ingersoll, 2016). Many studies have concentrated on constraining the outgassed mass flow rates (Burger et al., 2007; Dong et al., 2011; Hansen et al., 2006, 2008, 2011; Saur et al., 2008; Smith et al., 2010; Tenishev et al., 2010, 2014; Tian et al., 2007; Waite et al., 2006; Yeoh et al., 2015, 2017) using various physical models of the geysers. Examples include ballistic geysers from a point source based on three source parameters (the number density at the source, the flow speed, and the source temperature) and the orientation and location of the source (Dong et al., 2011), analytic solutions of the geyser particle velocity fields (Teolis et al., 2017) using the number density expression from Dong et al. (2011), and simple Direct Simulation Monte Carlo (DSMC) models (Portyankina et al., 2016, 2022; Spitale et al., 2015; Tucker et al., 2015).

The current study is an application of previous work by Mahieux et al. (2019), which presents state-of-the-art calculations and parametrizations of axisymmetric geyser flow fields using fully spatially and temporally resolved comprehensive DSMC simulations at steady-state. Mahieux et al. (2019) considered a single geyser, outgassing water vapor and single particle size pure water-ice grains, expanding into vacuum at supersonic speed in a steady state regime up to an altitude of 10 km, where the flow is essentially non-collisional. They parametrized the flow field characteristics, that is, number density, velocity, and temperature, at the 10-km upper boundary as a function of the vent conditions: mass flow rate, vent radius, water vapor exit speed, ice grain exit speed, mixture temperature, mass ratio between the two phases of water, size of the ice grains, and spreading angle. They then built functional forms to robustly and quickly reconstruct the flow field characteristics for any vent condition within a given range, defined based on physically plausible conditions.

In the present work, we aim to study whether the considered ground conditions of the vents can be inferred from the in situ Ion and Neutral Mass Spectrometer (INMS) and remote-sensing Ultraviolet Imaging Spectrograph (UVIS) observations, considering the location and orientation of the 98 vents described in Porco et al. (2014). INMS reported measurements of the local water vapor content sampled along the orbit of Cassini as it flew through the plumes. We uploaded the INMS Cassini trajectory data from the PDS online archive and used the water vapor local number density from Perry et al. (2015). UVIS performed solar (and stellar, not considered in this work) occultations of the plumes, from which the team derived integrated column densities as a function of the spacecraft's position and a look direction (Portyankina et al., 2018). We use the aforementioned functional forms as lower boundary conditions to simulate the flow at altitudes above 10 km, assuming collisionless flow conditions and considering the main external forces in an Enceladus-fixed reference frame. We model the INMS and UVIS observations of the Enceladus plumes. We fitted the INMS and UVIS data to the synthetic model we developed using the Levenberg-Marquardt least-squares algorithm. An unsuccessful attempt to fit the data using Markov Chain Monte Carlo is discussed in Appendix E in Supporting Information S1.

In this work, we show that in addition to the mass flow rates of various vents, some information regarding the ground conditions (mixture exit temperature and the size of the ice particles) can be constrained using the UVIS and INMS data for several vents, providing insights into underground physics and chemistry. A subsidiary result of this work is a fast and reliable method for determining which of the many physical parameters of a physically realistic plume model can be constrained by limited observational data, considering only the geometry of the observation.

21699100, 2025, 9, Downloaded from https://agupubs.onlinelibrary.wiley.com/doi/10.1029/2025JE009008 by Dtsch Zentrum F. Luft-U. Raum Fahrt In D. Helmholtz Gemein., Wiley Online Library on [18/08/2026]. See the Terms and Conditions (https://onlinelibrary.wiley.com/terms-and-conditions) on Wiley Online Library for rules of use; OA articles are governed by the applicable Creative Commons License

21699100, 2025, 9, Downloaded from https://agupubs.onlinelibrary.wiley.com/doi/10.1029/2025JE009008 by Dtsch Zentrum F. Luft-U. Raum Fahrt In D. Helmholtz Gemein., Wiley Online Library on [18/08/2026]. See the Terms and Conditions (https://onlinelibrary.wiley.com/terms-and-conditions) on Wiley Online Library for rules of use; OA articles are governed by the applicable Creative Commons License

Section 2 describes the method we use to expand the flow into space. We present a model Monte Carlo study of the sensitivity of the measuring instrument signals to several vent parameters in Section 3 and rank these parameters by their sensitivity to the observation geometry. Section 4 discusses the results obtained using a least-squares algorithm of the most sensitive vent parameters for the E3, E5, E7, E14, E17, and E18 INMS observations and the UVIS solar occultation. Finally, we present our conclusions in Section 5.

2. Flow Field Calculation

2.1. Parametrized Radial Profiles at 10 km Altitude

We first summarize the work presented by Mahieux et al. (2019). They performed detailed state-of-the-art simulations of the entire flow field of axisymmetric plumes and derived functional forms, which provide the number density, the radial and vertical velocities, and the kinetic temperature for water vapor and single particle size pure ice grains at 10 km altitude above a vent. These 10 km flow field conditions are used in this work as the lower boundary conditions of the simulations described in Section 2.2. Their analytical expressions of the parameterized radial profiles were calculated from comprehensive and fully spatially and temporally resolved DSMC simulations obtained using the code PLANET, which assumes that (a) the mass flow is composed of a mixture of water vapor and uniform-radius, water-ice particles exiting the ground at two independent supersonic speeds for each water phase, at a given mass ratio between water vapor and water-ice grains and uniform temperature, (b) the flow does not experience any force beside Enceladus's gravity g_E, (c) the vent is circular, (d) the flow exits the moon's surface with cylindrical symmetry relative to the axis normal to the vent center, (e) Enceladus has no atmosphere, (f) there are only neutral particles and the influence of electromagnetic fields is neglected, (g) as the composite flow exits through the vent, it spreads over an angle ("spreading angle") that varies uniformly from the vertical vent centerline to a maximum value at the vent edge to represent the initial flow, and (h) a single particle size—or mono-dispersed population—is an adequate approximation of true grain size distribution.

Assumption (f) is valid for large ice particles but might not always be true for particles with radii smaller than 1 μm, where charging can significantly affect their trajectories. However, the importance of charged sub-micron particles depends on their fraction in the plume. If it is small, they may be ignored as the neutrals would dominate the flow. Small charged particles would be swept away immediately by the swiftly rotating magnetosphere, leaving the neutral plume free of their influence. Additionally, for charged particles to play a significant role in the plume, their flux must be high enough to charge sub-micron neutrals there. At Enceladus' distance from Saturn, the flux of trapped charged particles is low. Moreover, the rings act as a sink for charged particles by sweeping out large volumes. Therefore, there is reasonable justification for considering the neutrals-only case.

As already noted in Mahieux et al. (2019), our plume-flow framework adopts, for reasons of tractability, assumption (h): a single particle size or monodisperse population of water-ice grains is used at the vent exit, that is, all particles are assigned a single representative radius. From a purely physical standpoint, this is, of course, an approximation. Direct and indirect evidence from Cassini Plasma Spectrometer (CAPS), Cosmic Dust Analyzer (CDA), Visible and Infrared Mapping Spectrometer (VIMS), and ISS investigations, as well as the condensation and wall-erosion scenarios outlined in Dong et al. (2015), show that Enceladus actually produces multiple grain populations whose characteristic sizes depend on their formative pathway: nanometer-scale condensates nucleated in the rapidly cooling vapor, sub-micron grains formed by homogeneous nucleation deeper in the conduit, and larger-than-micron fragments ablated from warm fracture walls (Ershova et al., 2024; Kempf et al., 2008; Waite et al., 2017). Collisions between these grains and the surrounding water molecules in the dense near-vent region do, in principle, affect momentum and energy exchange: the collision rate scales with the number density of grains, which itself scales inversely with the cube of grain radius at fixed mass flux, and thus modifies the early acceleration of both phases.

Yet, several pragmatic considerations argue for retaining a single effective grain size in the present study. First, the data sets we exploit, namely INMS local water-vapor number densities and UVIS column densities, are not directly sensitive to the microphysical grain-size spectrum. What these instruments do sense is the large-scale shape—and integrated density for UVIS—of the vapor plume. Numerical computations in Mahieux et al. (2019) demonstrate that once the flow has expanded beyond the first few meters where most collisions occur, the gross vapor field that determines the INMS/UVIS signal varies by only a few percent across a realistic

21699100, 2025, 9, Downloaded from https://agupubs.onlinelibrary.wiley.com/doi/10.1029/2025JE009008 by Dtsch Zentrum F. Luft-U. Raum Fahrt In D. Helmholtz Gemein., Wiley Online Library on [18/08/2026]. See the Terms and Conditions (https://onlinelibrary.wiley.com/terms-and-conditions) on Wiley Online Library for rules of use; OA articles are governed by the applicable Creative Commons License

Table 1
List of the Confidence Intervals for the Vent Parameters, Location, and Orientation

Vent parameter	Symbol	Units	Scale	Relative/absolute value	Default value	Min value	Max value
Mass flow rate	$\dot{m}$	[kg/s]	Linear	Absolute value	4.81	0	100
Water vapor speed	$v_{gas,ini}$	[m/s]	Linear	Absolute value	902	271	1,082
Water-ice speed	$v_{ice,ini}$	[m/s]	Linear	Absolute value	902	271	1,082
Vent radius	r_{vent}	[m]	Linear	Absolute value	1.4	0.2	6.0
Ice grain mass ratio	f_{ice}	[-]	Linear	Absolute value	5	0	0.5
Ice grain radius	r_{ice}	[μm]	Log	Absolute value	1	0.01	5
Mixture temperature	T_{ini}	[K]	Linear	Absolute value	53	33	143
Vent spreading angle	α_v	[°]	Linear	Absolute value	0	0	9
Vent latitude	L	[°]	Linear	Relative value	0	−0.32	+0.32
Vent longitude	l	[°]	Linear	Relative value	0	−0.32	+0.32
Vent zenith angle	θ_Z	[°]	Linear	Relative value	0	−0.8	+0.8
Vent azimuth angle	θ_A	[°]	Linear	Relative value	0	−0.8	+0.8

Note. The fourth and fifth columns refer to the scales used to calculate the random values: linear or logarithmic scales and absolute or relative values. The relative values are calculated relative to the location and orientation of the vents, as reported by Porco et al. (2014).

range of grain radii. Put differently, the vapor phase dominates the observables at Cassini altitudes, and the details of the size distribution imprint only second-order perturbations.

Second, allowing each vent to possess its own grain-size distribution (modal radius, width, multiple modes) would dramatically multiply the parameter count. Such a high-dimensional search space is severely under-constrained by relatively few measurement points available per fly-by, leading to unstable fits or indeterminate solutions.

Finally, our objective is to identify which gas-phase vent conditions can be constrained solely from vapor observations. Instruments that are directly sensitive to grain size, such as CDA, are outside the scope of the current work. Incorporating those measurements in future studies would indeed warrant revisiting the full multi-population description.

In summary, while a multi-modal grain-size distribution is undoubtedly more realistic, adopting a single representative radius is a justified compromise. It preserves the dominant gas–particle coupling that shapes the macroscopic plume, keeps the inversion problem computationally manageable, and avoids introducing poorly constrained variables that the INMS and UVIS data simply cannot resolve. We therefore retain the single particle size assumption here, but we explicitly acknowledge that future analyses integrating CDA or next-generation in situ dust detectors could and should treat the full size spectrum explicitly (see Section 3 for further discussion).

The vertical domain of the DSMC computation extends from the surface up to 10 km altitude, where the gas mixture was shown to be collisionless, that is, the gradient-based Knudsen number, K_n, is much larger than 1 for both gas and grains. This is the case for the entire range of vent parameters considered here and in Mahieux et al. (2019). Only a 1° azimuthal cylindrical slice of the flow was computed with respect to the axis normal to the surface passing through the center of the vent under the assumptions listed above.

Mahieux et al. (2019) considered the vent parameters in Table 1 as the "default" or nominal vent parameters. They were obtained from previous work conducted by our group at The University of Texas at Austin and summarized by Yeoh et al. (2017). The analytical expressions of the parametrizations are described in detail in Appendix A in Supporting Information S1. It should be noted that the computation of a single DSMC simulation from surface to 10 km altitude takes up to 48 hr using 4 CPUs (on Intel E5-2690 v3 12-core machines), while the reconstruction of the radial profile at 10 km using the parametric fits only takes a fraction of a second on the same machine—this is the key benefit of creating the parametric fit. As discussed in Mahieux et al. (2019), the significant computation time saved is obtained at the cost of reduced precision of the density and velocity profiles at 10 km altitude when compared to the DSMC calculations for random vent parameter values. The fields obtained using the above-described parametrizations generally agree with the corresponding full DSMC simulations to within 5%. In the worst case, they differ by 20%.

2.2. Expansion of the Plume at Higher Altitude

We compute the further expansion of the plumes toward space using the analytical curve fit expressions for the flow fields at an altitude of 10 km as the lower boundary condition. We define a rotating reference frame with the origin at the center of Enceladus and the x-axis pointing toward Saturn—because Enceladus is tidally locked in its orbit around Saturn, the z-axis pointing toward Enceladus' North, and the y-axis such that the axis system is right-handed. We assume here that (a) Enceladus's orbital plane and Saturn's equatorial plane coincide (the inclination angle between the two planes is negligible at 0.019°), (b) the orbit of Enceladus around Saturn is circular—the orbital eccentricity is extremely small (0.0047), (c) the rotation axis of Enceladus is normal to its orbital plane, and (d) Saturn is a spherical body.

In the above-defined Enceladus rotating reference frame, the particles are subject to different accelerations: $\boldsymbol{g_E}$ and $\boldsymbol{g_S}$, relative to the Enceladus and Saturn gravity fields, $\boldsymbol{a_E}$ the centrifugal acceleration due to the orbit of Enceladus around Saturn, and the Coriolis and centrifugal accelerations due to Enceladus' self-rotation $\boldsymbol{\omega_E}$.

If $\boldsymbol{r} = (x, y, z)$ denotes the position of a particle, $(\boldsymbol{e_x}, \boldsymbol{e_y}, \boldsymbol{e_z})$ are the unit vectors of the right-handed coordinate system, and $\boldsymbol{e_r}$ the unit radial vector, we can write the equation of motion of a particle (Kempf et al., 2010; Yeoh et al., 2017):

$$\ddot{\boldsymbol{r}} = \boldsymbol{g_E} + \boldsymbol{g_S} + \boldsymbol{a_E} - 2\,(\boldsymbol{\omega_E} \times \dot{\boldsymbol{r}}) - \boldsymbol{\omega_E} \times (\boldsymbol{\omega_E} \times \boldsymbol{r}) \tag{1}$$

where $\boldsymbol{g_E} = -\frac{\mu_E}{r^2}\,\boldsymbol{e_r}$ is the gravitational acceleration from Enceladus, with μ_E the product of the universal gravitational constant and the Enceladus mass ($\mu_E = 7.21 \times 10^9\ \mathrm{m^3/s^2}$), $\boldsymbol{g_S} = -\frac{\mu_S}{\|(\boldsymbol{r} - d_{ES}\ \boldsymbol{e_x})\|^2}\,\frac{(\boldsymbol{r} - d_{ES}\ \boldsymbol{e_x})}{\|(\boldsymbol{r} - d_{ES}\ \boldsymbol{e_x})\|}$ is the gravitational acceleration due to Saturn, where d_{ES} is the distance between Enceladus and Saturn ($d_{ES} = 238{,}020$ km and $\mu_S = 3.798 \times 10^{16}\ \mathrm{m^3/s^2}$ is the product of the Enceladus mass and the universal gravitational constant), $\boldsymbol{a_E} = -\left(\frac{2\pi}{\tau_E}\right)^2 d_{b_{ES}}\,\boldsymbol{e_x}$ is the centrifugal acceleration due to the orbit of Enceladus around Saturn, where $\tau_E = 1.18 \times 10^5$ s is the Enceladus orbital period and $d_{b_{ES}}$ is the distance between the Saturn-Enceladus system barycenter and the Enceladus mass center, which is nearly equal to d_{ES} (relative difference of the order of 10^{-7}), $2\,(\boldsymbol{\omega_E} \times \dot{\boldsymbol{r}})$ is the Coriolis acceleration, where $\boldsymbol{\omega_E} = \omega_E\,\boldsymbol{e_z}$ and $\omega_E = \frac{2\pi}{\tau_E}$, and $\boldsymbol{\omega_E} \times (\boldsymbol{\omega_E} \times \boldsymbol{r})$ is the centrifugal acceleration due to Enceladus' self-rotation. Even though we include all force terms in the simulations described below, the terms $\boldsymbol{g_E}$ and $2\,(\boldsymbol{\omega_E} \times \dot{\boldsymbol{r}})$ are the more important ones.

Appendix B in Supporting Information S1 provides details on the analytical and free-molecular methods. It also provides two applications to simple cases, one for INMS observation configuration and one for UVIS, and a comparison between the analytical solution and the solution from a free molecular code.

3. Vent Parameter Sensitivity Study

3.1. Introduction

In this work, we focus exclusively on the 98 vent positions and orientations reported by Porco et al. (2014). These vents were identified using high-resolution Cassini ISS imaging, with their locations and directions triangulated from resolved particulate jets. This catalogue remains the most spatially complete and geometrically constrained data set available for the Enceladus South Polar Terrain. Alternative indicators of vent activity—such as thermal anomalies from CIRS (Howett et al., 2011; Spencer et al., 2006) or compositional signatures from INMS or CDA (Magee and Waite., 2017; Waite et al., 2006, 2017)—offer complementary insights but typically lack either the spatial coverage, positional accuracy, or directional information required for the present modeling approach. Using this uniform and well-characterized vent set allows us to consistently apply our sensitivity and inversion framework across all observations.

Our final goal is to obtain, for as many of the 98 geysers as possible, the vent parameters listed in Table 1 to which an observation geometry is sensitive, that is, that could be further constrained. We note that the logarithm of the ice grain radius is fitted, as this form was also used in the parametrization of the flow fields presented in Mahieux

21699100, 2025, 9, Downloaded from https://agupubs.onlinelibrary.wiley.com/doi/10.1029/2025JE009008 by Dtsch Zentrum F. Luft-U. Raum Fahrt In D. Helmholtz Gemein., Wiley Online Library on [18/08/2026]. See the Terms and Conditions (https://onlinelibrary.wiley.com/terms-and-conditions) on Wiley Online Library for rules of use; OA articles are governed by the applicable Creative Commons License

10.1029/2025JE009008

et al. (2019). Also, if sensitive to these variables, the water vapor and water ice speeds are fitted separately, as their respective speeds were reported to be different (Ershova et al., 2024; Kempf et al., 2010; Postberg et al., 2011; Schmidt et al., 2008), even though their respective boundaries in Table 1 are equal. We also consider potential adjustments to the latitude/longitude of the vents and the azimuth and zenith angles of their pointing directions listed in Porco et al. (2014), according to the uncertainties provided in Table 2 of the reference: we allow the vent latitude and longitude to vary by $\pm 0.32°$ and the azimuth and zenith angles by $\pm 0.8°$ from the reported values. In the remainder of the text, we include the location and orientation of each vent under the designation of "vent parameter." That is, we have a list of 12 parameters to consider per vent, or 1,176 free variables in total for the 98 vents. Each INMS or UVIS observation has between 10 and 125 measurement points sampled at different locations along the Cassini flight path, and the UVIS occultation has ∼100 column-integrated values, leading to under-constrained fits.

The latter motivates the implementation of specific methods to determine the vent parameters that likely contribute to a particular observation and should be considered in a subsequent fitting procedure. To reduce the size of the problem, since a single plume computation only takes a few seconds, we use a Monte Carlo statistical method (Higdon et al., 2017) and calculate correlation probabilities using the Pearson algorithm, available in MATLAB and thoroughly described in Appendix C in Supporting Information S1, to a given Quantity of Interest (QoI). For the QoI, we use the simulated water vapor number density at each INMS measurement point along the trajectory or the integrated water vapor column density at each UVIS measurement point. We note that this work does not include any contribution from material originating from the E-ring, which adds a diffuse continuum to the measured signal of the various instruments (see Postberg et al. (2009), Tenishev et al. (2024), and Yeoh et al. (2015) e.g.).

In this section, we apply the Pearson correlation coefficient method to the vent parameters without considering the physical dependence of these parameters on the flow conditions. An essential advantage of this method, as compared to methods that vary one parameter at a time while considering all other parameters constant, is that one can isolate the relative importance of a given parameter within a complex system driven by many parameters while effectively canceling the effects of all the others—since all parameters are varied simultaneously and randomly. We vary each parameter over the ranges given in Table 1 and arbitrarily set a threshold value to 0.01 to determine whether an observation is sensitive to a given vent parameter. The ranges were designed to encompass the broadest possible physically plausible values for each parameter as discussed by Mahieux et al. (2019). We illustrate our approach, discuss its validity, and examine the sample size needed to correctly calculate the correlations in a simple case, considering simplified observation geometry in Appendix C in Supporting Information S1.

Given the high dimensionality of the problem and the limited number of observational constraints, multiple parameter reduction strategies are possible. In this work, we chose to fit only those vent parameters that showed meaningful sensitivity to the specific observation geometry, while fixing the remaining parameters to values derived from Yeoh et al. (2015). This choice was motivated by numerical stability considerations for the fitting algorithm presented in Section 4 as well as the desire to preserve local variability in parameters where sufficient sensitivity exists. Alternative strategies, such as assuming a single global value for certain vent parameters (e.g., grain size or exit speed), could provide a more constrained framework but may mask localized physical differences or temporal variability. Since previous studies have shown time variability in mass flow rate associated with tidal forcing, it is reasonable to expect other vent properties to vary as well. Our approach aims to capture these potential differences without overfitting the available data. Future work may compare alternative parameter reduction strategies to assess the robustness of the retrieved plume characteristics.

3.2. Sensitivity to the 98 Geyser Vent Parameters

We consider the actual orbit configurations of six INMS observations (E3, E5, E7, E14, E17, and E18) and the UVIS solar occultation, together with the vent positions and orientations given by Porco et al. (2014).

We present the vent parameter correlation coefficients obtained using the abovementioned Pearson method for these observations. The total number of vent parameters for each observation geometry corresponds to the number of non-zero observation points to avoid under-constraining the problems, as reflected by the equal numbers provided in columns "Number of observation points" and "Total number of variables" for each observation in Table 2.

21699100, 2025, 9, Downloaded from https://agupubs.onlinelibrary.wiley.com/doi/10.1029/2025JE009008 by Dtsch Zentrum F. Luft-U. Raum Fahrt In D. Helmholtz Gemein., Wiley Online Library on [18/08/2026]. See the Terms and Conditions (https://onlinelibrary.wiley.com/terms-and-conditions) on Wiley Online Library for rules of use; OA articles are governed by the applicable Creative Commons License

Table 2
Number of Vent Parameters by Category for Each Observation Geometry

Instrument	Observation	Number of observation points	Mass flow rate	Gas speed	Ice grain speed	Vent radius	Ice grain diameter	Mass ratio	Spreading angle	Temperature	Latitude	Longitude	Azimuth	Zenith	Total number of variables
INMS	E3	17	17	–	–	–	–	–	–	–	–	–	–	–	17
	E5	10	10	–	–	–	–	–	–	–	–	–	–	–	10
	E7	37	37	–	–	–	–	–	–	–	–	–	–	–	37
	E14	125	96	–	1	6	4	1	–	3	2	6	3	3	125
	E17	105	85	–	1	5	3	1	–	3	2	2	1	2	105
	E18	119	90	–	1	6	4	1	2	3	1	7	2	2	119
UVIS	SO	105	98	–	–	–	–	–	–	2	–	2	2	1	105

21699100, 2025, 9, Downloaded from https://agupubs.onlinelibrary.wiley.com/doi/10.1029/2025JE009008 by Dtsch Zentrum F. Luft-U. Raum Fahrt In D. Helmholtz Gemein., Wiley Online Library on [18/08/2026]. See the Terms and Conditions (https://onlinelibrary.wiley.com/terms-and-conditions) on Wiley Online Library for rules of use; OA articles are governed by the applicable Creative Commons License

10.1029/2025JE009008

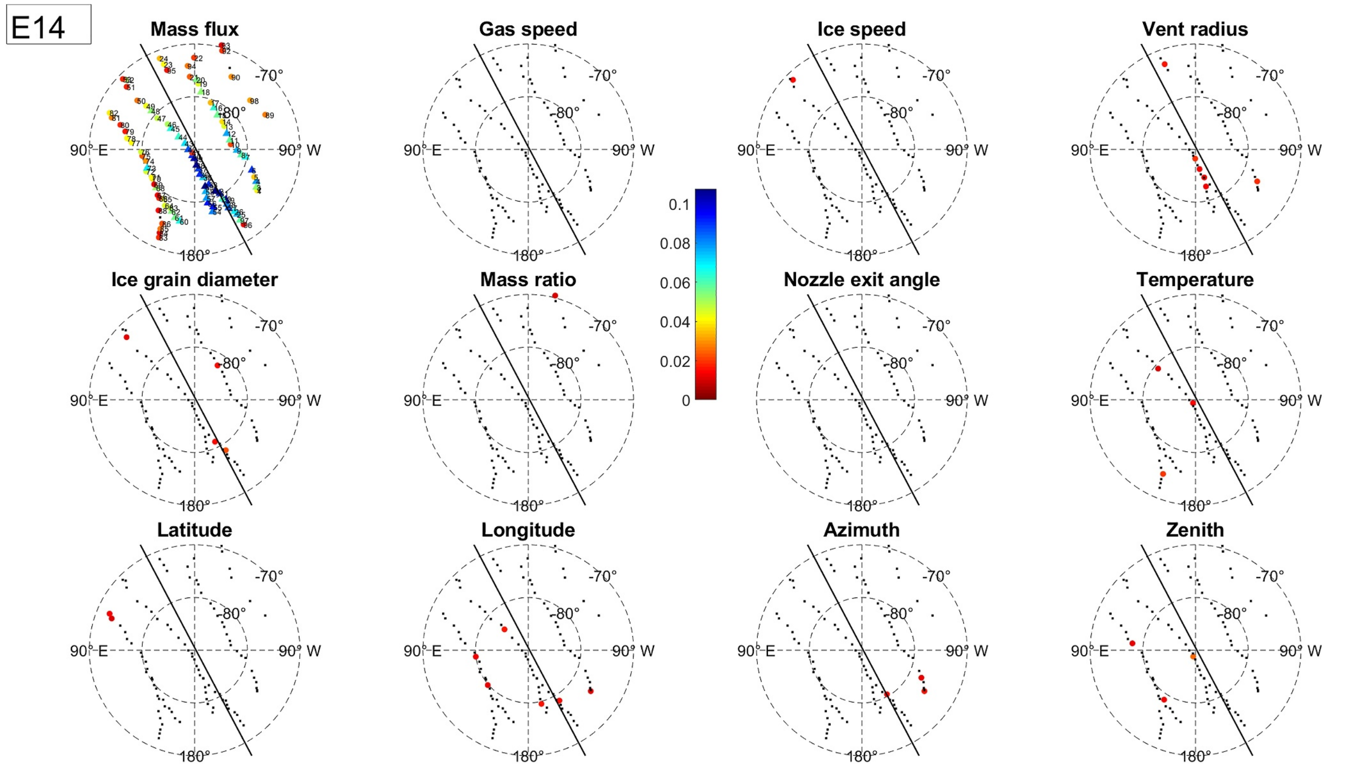

Figure 1. South polar view of the mean correlation of the vent parameters to the Ion and Neutral Mass Spectrometer E14 observation geometry, where each symbol represents the position of the vents reported by Porco et al. (2014), and the color code is the mean correlation value (see color bar). The black line represents the projection on the surface of the Cassini spacecraft trajectory. The parameters correlated with values greater than 0.05 are triangles, lower are circles, and the uncorrelated parameters are black points.

The mean correlation values for the INMS observations are depicted graphically in Figure 1 for E14 and in Appendix C in Supporting Information S1 for the other observation geometries; see Figures C2 to C6. The mean correlation values are also tabulated in Appendix C in Supporting Information S1 for all observation geometries; see Tables C2 to C8. The number of correlated parameters for each observation—those whose mean correlation value exceeds 0.01—is summarized in Table 2.

As an example, we consider the sensitivity to observation E14, presented in Figure 1, which had its closest approach at an altitude of 95 km and a latitude of −89°, with the spacecraft path nearly parallel to the main direction of the Tiger Stripes in a Southwest-Northeast configuration. Ninety-six vent parameters show a confident correlation (with a correlation value larger than 0.01) to mass flow rate, one to ice grain speed, six to vent radii, four to ice grain diameter, one to the water phase mass ratio, three to the exit temperature, and 14 to either location or orientation components. Thus, we can now rank the vent parameters that contribute the most to mass flow rate, vent radius, ice grain exit speed, etc., for each observation to the measured INMS local water vapor number density.

The mean correlation coefficients for mass flux decrease with lateral distance from the spacecraft ground track, as expected from the rapid radial fall-off of plume density: vents nearest the line of sight contribute most strongly to the measured signal. In contrast, parameters such as the ice-to-vapor mass ratio or grain exit speed show isolated non-zero correlations only where the trajectory skims the edge of a vent's plume cone; these kinds of hot spots mark locations of locally enhanced sensitivity, whereas most vents remain unconstrained. Finally, comparing flybys E14 (Figure 1) and E7 (Figure C4 in Supporting Information S1) illustrates the role of trajectory orientation: E14's ground track lies nearly parallel to the Tiger Stripes and therefore samples multiple vents along their principal axis, resulting in broad sensitivity to both mass flux and vent radius. In contrast, E7 traverses the stripes nearly perpendicular to their strike, sampling each plume in cross-section and producing a more localized and parameter-specific correlation pattern. These differences underscore how the spacecraft's path relative to the fracture geometry controls which vent parameters can be constrained.

21699100, 2025, 9, Downloaded from https://agupubs.onlinelibrary.wiley.com/doi/10.1029/2025JE009008 by Dtsch Zentrum F. Luft-U. Raum Fahrt In D. Helmholtz Gemein., Wiley Online Library on [18/08/2026]. See the Terms and Conditions (https://onlinelibrary.wiley.com/terms-and-conditions) on Wiley Online Library for rules of use; OA articles are governed by the applicable Creative Commons License

Regarding the other INMS observations, similar conclusions can be drawn. The spacecraft flew far from the satellite for the E3 (Figure C2 in Appendix C in Supporting Information S1) and E5 (Figure C3 in Supporting Information S1) observation geometries. The closest approach occurred at an altitude of 49.1 km and latitude of −20° for E3 and 2525 km and −2828° for E5; thus, both were far from the South Polar Region. The minimum distance between the spacecraft and the South Pole was 225 km for E3 and 162 km for E5 due to a large angle relative to the Enceladus equatorial plane of the Cassini orbit. In addition, the mean speed of the spacecraft with respect to Enceladus for E3 and E5 was also larger than during E7: 14.4 and 17.7 km/s, respectively, which limited the number of sampling points. Consequently, INMS sampled the geysers far away from the moon and at a relatively large speed, resulting in a poorer data set. Consequently, the mass flow rate of 17 vents is correlated with the observation geometry for E3 and of 10 vents for E5. INMS E7 presents similar results. It had its closest approach at an altitude of 96 km and a latitude of −87°, with the spacecraft path following a South West–North East ground track that intersected all four Tiger Stripes at a steep crossing angle, rather than running parallel to them. The mean speed of the spacecraft with respect to Enceladus during the measurement period was 7.7 km/s. The observation geometry is sensitive to the mass flow rates of 37 vents. We cannot infer information about the other vent parameters from these three observations.

The E17 and E18 observation geometries are similar to that of E14, as the spacecraft was flying on an orbit nearly parallel to the Enceladus Equatorial plane, at a minimum distance from the satellite of 72 km for E17 and 71 km for E18, located close to the South Pole (−87° and −88° respectively) and at low relative mean speed (~7 km/s). They also occurred on a flight path nearly parallel to the main direction of the Tiger Stripes. Similar conclusions can be drawn for E14: correlations to the mass flow rate of many vent parameters are obtained (85 and 90, respectively), and to some other vent parameters, 19 for E17 and 29 for E18. Besides being sensitive to the mass flow rates, we see that some information relative to nearly all other vent parameters (besides the water vapor exit speed) could theoretically be obtained from remote sensing observations, retrieving only information on the water vapor number density.

Finally, we consider the UVIS solar occultation observation, which sampled the whole plume system, measuring column-integrated water vapor densities. The results related to the sensitivity study of the vent parameters are presented in Figure C7 in Appendix C in Supporting Information S1. The Sun was located to the Northwest, while the spacecraft was orbiting in the Southeast. The sensitivity analysis returns correlations to all 98 vent mass flow rates. This is related to the fact that during the solar occultation, due to the sampling technique, UVIS accounted for the contribution of all geysers, in contrast to INMS observation, which sampled local densities. In addition, the observation was sensitive to the exit temperature of two vents and the location and orientation of five vents.

It is important to note that given the large number of vent parameters and the limited number of measurement points per observation, the system is inherently under-constrained. While the Pearson correlation method allows us to identify potentially sensitive parameters, weak correlations—especially those limited to a few vents far from the observation path—may not always reflect robust physical constraints. Rather, they may arise from statistical variability or complex interactions within the high-dimensional parameter space. To mitigate this, we apply a minimum threshold of 0.01 to the mean correlation coefficient and consider only parameters whose correlations are statistically significant (p-value <0.05). We interpret strong and spatially coherent correlations as likely indicators of physical sensitivity, particularly when they appear consistently across neighboring vents or multiple observations. In contrast, isolated weak correlations, especially for parameters other than mass flow rate, are presented as tentative indications of potential sensitivity and should be interpreted with caution. Nevertheless, for some observations that have more observation points, notably E14, E17, E18, and UVIS, we find meaningful sensitivity to a range of parameters beyond the mass flow rate, such as vent radius, exit temperature, and orientation, suggesting that these properties can, in favorable configurations, be partially constrained by remote sensing or local sampling of the water vapor number density fields.

The results presented in this section are based on Cassini observation geometries, which were limited in spatial and temporal coverage. In the following section, we explore how the same methodology could be used prospectively to support observation planning for future missions, where flyby geometries and measurement strategies can be optimized.

21699100, 2025, 9, Downloaded from https://agupubs.onlinelibrary.wiley.com/doi/10.1029/2025JE009008 by Dtsch Zentrum F. Luft-U. Raum Fahrt In D. Helmholtz Gemein., Wiley Online Library on [18/08/2026]. See the Terms and Conditions (https://onlinelibrary.wiley.com/terms-and-conditions) on Wiley Online Library for rules of use; OA articles are governed by the applicable Creative Commons License

21699100, 2025, 9, Downloaded from https://agupubs.onlinelibrary.wiley.com/doi/10.1029/2025JE009008 by Dtsch Zentrum F. Luft-U. Raum Fahrt In D. Helmholtz Gemein., Wiley Online Library on [18/08/2026]. See the Terms and Conditions (https://onlinelibrary.wiley.com/terms-and-conditions) on Wiley Online Library for rules of use; OA articles are governed by the applicable Creative Commons License

Table 3
Total Fitted Mass Flow Rate for the Six Ion and Neutral Mass Spectrometer Observations and the Ultraviolet Imaging Spectrograph Solar Occultation and Number of Fitted Vents' Mass Flow Rates

Observation	Total mass flow rate	Number of free vent parameters	Number of fitted active vents
INMS E3	135 ± 34 kg/s	17	17
INMS E5	204 ± 37 kg/s	10	10
INMS E7	109 ± 15 kg/s	37	37
INMS E14	426 ± 54 kg/s	82	76
INMS E17	486 ± 50 kg/s	69	66
INMS E18	403 ± 13 kg/s	51	51
UVIS Solar Occ.	217 ± 24 kg/s	103	98

3.3. How This Approach May Serve as an Operational Tool for Future Space Missions That Involve Observations of Cryovolcanic Activity

The approach presented in this section provides the ability to compute the number density and velocity fields of cryovolcanic plumes rapidly and precisely up to hundreds of kilometers above the surface and to estimate the resulting sensitivity to the vent parameters. A reduction in the computation time by four orders of magnitude compared to DSMC and to free molecular simulations has been demonstrated, while the accuracy of the simulations degraded generally by less than 5%—and up to 20% in the worst-case scenarios—relative to full DSMC and free molecular simulations.

Future missions to Enceladus or Europa (Dayton-Oxland et al., 2023) or other icy satellites showing geysers will need to plan flyby and orbital trajectories that best sample and characterize those geysers based on presumed or known vent locations. The approach presented herein could be used during mission planning to predict what information could be constrained based on particular observation geometries and measurement techniques. This would include in situ observations with instruments similar to INMS or remote sensing observations such as occultations as observed by the UVIS instrument. If a particular vent radius, mass flow rate, or other property were of specific interest, the sensitivity approach described above may determine suitable trajectories, pointing directions, and sampling rates for the mission. Similarly, a related sensitivity study employing the same techniques could be undertaken if vehicle safety were an issue for a space mission to a satellite producing a substantial gas or particulate flux (e.g., Io). Reliable sensitivity maps could be quickly created for possible observation geometries (including spacecraft path, speed, and sampling rates) to maximize the mission's scientific outcome. We note that the approach provided in this section is limited to plumes on airless bodies where the gravity is too low to produce canopy shocks. Thus, it would also apply to the putative plumes that may exist on Europa (Dayton-Oxland et al., 2023).

4. Constraining the Vent Parameters

Here, we consider specific retrieval fitting techniques for particular vent conditions. We present the results of the sensitive vent parameters that fit the data measured by INMS and UVIS. To do so, we follow the procedure described in Appendix D in Supporting Information S1, which uses the Levenberg-Marquardt least-squares algorithm (Dentler, 2024). This procedure returns the maximum number of fitted parameters that do not underconstrain the problem to be solved and a robust evaluation of the uncertainty on each fitted parameter. We note that our original objective was to constrain the vent parameters using the Markov Chain Monte Carlo method, but this did not yield satisfactory results. This effort is summarized in Appendix E in Supporting Information S1.

We order the free vent parameters from five to the number of independent measurement points based on their sensitivity to the problem geometry. We perform a series of parametric fits while increasing the number of free vent parameters. We control the fit's root mean square (RMS) error and the total mass flow rate. Initially, these two quantities do not vary much from one set of vent parameters to the next; see Figure D1 in Appendix D in Supporting Information S1. Then, at some point, both quantities start to differ while the RMS error increases. The third column of Table 3 gives the number of successfully fitted parameters. Next, for each set of fitted variables,

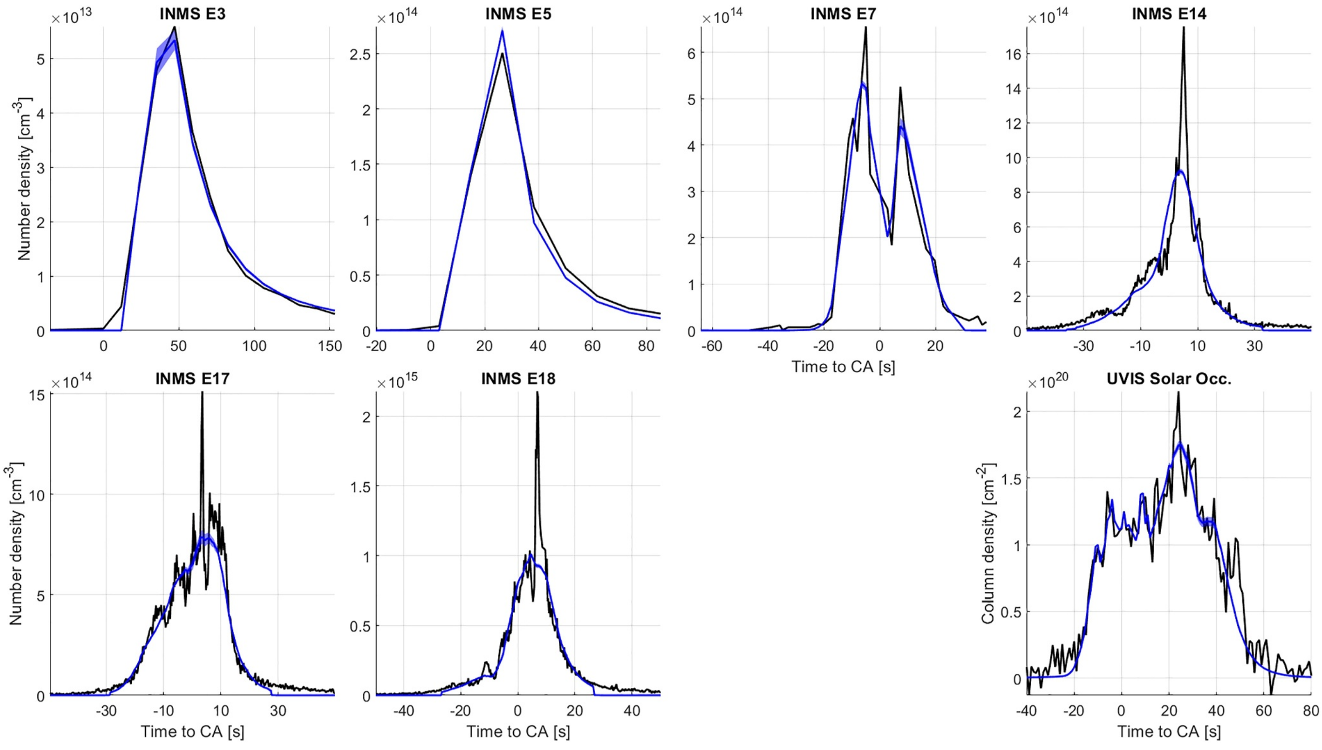

Figure 2. Results of the fits of the Ion and Neutral Mass Spectrometer E3, E5, E7, E14, E17, E18, and the Ultraviolet Imaging Spectrograph solar occultation. In each panel, the black curve is the observation, and the blue curve is the best fit, the width of which represents the uncertainty.

we evaluate the dependence on the a priori values used for the fit and the effect of the non-fitted variables on the quality of the fit. First, we check that the fit results are independent of the a priori values. Second, we compute one hundred fits in which the vent parameters that are not fitted for the active vents, that is, for which we fit the mass flow rate, are set to random values. We evaluate the variance in the resulting fitted parameters and add it to the uncertainty of the fitted free vent parameters. The way these effects are accounted for in the resulting fits is described in Appendix D in Supporting Information S1. This approach ensures that (a) the problem is not under-constrained, (b) that the total mass flow rate is consistent and robust since it varies little from one set of free vent parameters to the next one, (c) the computations are done based on robust and extensive DSMC computations that were parametrized in Mahieux et al. (2019), and (d) that the possible effect of the vent parameters that were not fit because of their weak influence on the observation (reflected in the sensitivity values), is accounted for in the procedure.

The results of the simulations using the fitted parameters are presented in Figure 2. The fits agree reasonably well with the Cassini observations. However, the simulation fails to reproduce the finer observed structure, most notably the spike/dip detected at 4–7 s after the closest approach in INMS E14, E17, and E18. When looking at the number density radial profiles computed by Mahieux et al. (2019) for any vent parameters within reasonable ranges (see Table 1), none presents such a narrow full width at half maximum. It is hard to understand what could cause that feature. One explanation given by previous authors is that the venting Mach number could be much larger (Goldstein et al., 2018), even though the processes that would create such large exit speeds are not yet understood. Another reason could be that it might be related to the presence of other gases in the degassed material. For example, H_2 was detected in the INMS data and presented very sharp profiles (Waite et al., 2017). Other gases were also detected in the plumes (Khawaja et al., 2019), but only water vapor and ice were included in the DSMC simulations that were run to produce the profiles at 10 km whose parametrizations are used here (Mahieux et al., 2019). Preliminary studies of the underground conditions in the fractures using DSMC and considering water vapor and H_2 show that narrow layers of both gases may be produced and might explain the unfitted observation (Zaharias et al., 2023). Near-surface jet-jet interactions could also produce such narrow beams (McDoniel et al., 2015), but these configurations are not considered in this work.

21699100, 2025, 9, Downloaded from https://agupubs.onlinelibrary.wiley.com/doi/10.1029/2025JE009008 by Dtsch Zentrum F. Luft-U. Raum Fahrt In D. Helmholtz Gemein., Wiley Online Library on [18/08/2026]. See the Terms and Conditions (https://onlinelibrary.wiley.com/terms-and-conditions) on Wiley Online Library for rules of use; OA articles are governed by the applicable Creative Commons License

Table 4
List of the Total Mass Flow Rates Found in the Literature in kg/s (Burger et al., 2007; Dong et al., 2011; Hansen et al., 2011; Smith et al., 2010; Teolis et al., 2017; Tian et al., 2007; Yeoh et al., 2017)

Observation	Mean anomaly	Burger et al. (2007)	Tian et al. (2007)	Smith et al. (2010)	Dong et al. (2011)	Hansen et al. (2011)	Teolis et al. (2017)—adiabatic	Teolis et al. (2017)—Non adiabatic	Yeoh et al. (2017)	This work
UVIS SO	98°					179 ± 48	648	436		217 ± 24
UVIS γ Ori	117°	300	150 ± 31			170 ± 16				
INMS E18	194°						922 ± 61	620 ± 39		403 ± 13
INMS E17	199°						688 ± 50	462 ± 34		486 ± 50
INMS E5	200°			749	1,045				900	204 ± 37
UVIS ζ Ori	236°					220 ± 21	732	489		
INMS E14	241°						737 ± 61	494 ± 42		426 ± 54
INMS E7	263°						402 ± 74	271 ± 47	450 ± 50	109 ± 15
INMS E3	274°			191	509				451	135 ± 34

The E3, E5, E7, E17, and E18 observations conducted by the INMS instrument only provided information on the total mass flow rate as reported in Table 3. The values obtained from this work are compared to those reported in the literature, which are listed in Table 4 and plotted in Figure 3.

The total mass flow rates reported in this work are, in general, lower than the ones reported in the literature for the INMS observations and never reach values larger than 486 kg/s, whereas other authors reported values up to 1,045 kg/s; see Dong et al. (2011). We explain these differences in terms of the different approaches that were taken by the various authors, including our approach here, where we simulate the plumes using robust DSMC simulations that account for molecular and particle collisions during the expansion into vacuum. The values measured during E0, E1, and E2 (Saur et al., 2008; Tenishev et al., 2014; Waite et al., 2006) are not reported in the above graph because of the much lower quality of the data sets compared to the ones considered in this study. Similar to what was presented in Teolis et al. (2017), the total mass flow rates are presented in Figure 3 as a function of the mean anomaly (i.e., the position of Enceladus in its orbit around Saturn) during the observation. The total mass flow rates derived in this work could depend on the mean anomaly, as Teolis et al. (2017) reported:

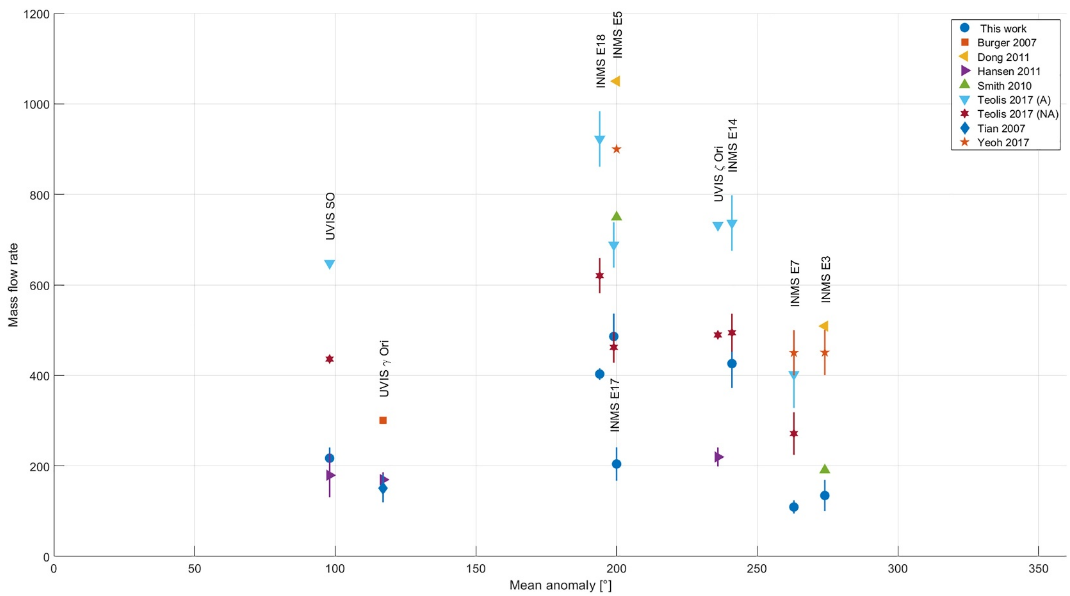

Figure 3. Comparison of the mean mass flow rates for all observations and with data from the literature (Burger et al., 2007; Dong et al., 2011; Hansen et al., 2011; Smith et al., 2010; Teolis et al., 2017; Tian et al., 2007; Yeoh et al., 2017). Teolis et al. (2017) (A) stands for the adiabatic results presented in that work, while Teolis et al. (2017) (NA) stands for the non-adiabatic ones.

21699100, 2025, 9, Downloaded from https://agupubs.onlinelibrary.wiley.com/doi/10.1029/2025JE009008 by Dtsch Zentrum F. Luft-U. Raum Fahrt In D. Helmholtz Gemein., Wiley Online Library on [18/08/2026]. See the Terms and Conditions (https://onlinelibrary.wiley.com/terms-and-conditions) on Wiley Online Library for rules of use; OA articles are governed by the applicable Creative Commons License

Table 5
Vent-Free Parameters Fitted From Ion and Neutral Mass Spectrometer E14 and the Ultraviolet Imaging Spectrograph Solar Occultation

Observation	Quantity	Vent number	Value
INMS E14	Ice grain diameter	29	1.1 ± 0.46 μm
INMS E14	Azimuth angle	40	0.125 ± 0.321°
UVIS Solar Occ.	Temperature	12	60.8 ± 15.7 K
UVIS Solar Occ.	Temperature	86	44.5 ± 11 K
UVIS Solar Occ.	Longitude	45	0.193 ± 0.003°
UVIS Solar Occ.	Azimuth angle	31	0.249 ± 0.18°
UVIS Solar Occ.	Zenith angle	40	−0.574 ± 0.004°

larger values are obtained when the mean anomaly is close to 180° and lower at 90° and 270°. In our study, the values at 180° mean anomaly seem to be variable, varying between 486 ± 50 and 204 ± 37 kg/s, while values at 90° and 270° mean anomaly have much lower mass flow rates, ranging between 217 ± 24 and 109 ± 15 kg/s.

Our results show that total fitted mass flow rates vary between successive flybys, which may reflect changes in vent activity. This is consistent with previous findings from remote sensing observations, particularly ISS and VIMS data, which revealed a strong correlation between plume brightness and Enceladus' mean anomaly (Hedman et al., 2013; Ingersoll & Ewald, 2017; Nimmo et al., 2014). Additionally, Hansen et al. (2020) analyzed the complete set of UVIS stellar occultations and derived H_2O column densities and gas production rates consistent with a structured and variable plume. Their results confirm that significant variability in plume output exists across different flybys, with production rates typically ranging from ∼150 to 300 kg/s, broadly consistent with the values inferred from INMS and CDA data, and in agreement with the values reported in this work.

The E14 INMS observation and the UVIS solar occultation provide information on the total mass flow rate and a few other vent parameters: the ice grain diameter and azimuth angle of one vent for INMS E14, the temperature of two vents, the longitude of one vent, the azimuth angle of another vent, and the zenith angle of another one. The values are listed in Table 5. Unfortunately, our technique could not infer information on the other vent parameters, that is, the vent radii, spreading angle, water vapor and ice grains exit speeds, and mass fraction between the two water phases.

The temperature fitted for two vents during the UVIS solar occultation (60.8 ± 15.7 K and 44.5 ± 11 K) indicates that the water mixture exits the vents at a low temperature (53 K), which means that the a priori value considered in our work is a good guess. The initial temperature of the mixture alters the flow as it gives it more or less energy to expand over the first few vent diameters above the surface. No temperature estimation of the outgassed mixture could be found in the literature. However, the surface temperature of the ground around the crevasses could be modeled using CIRS and VIMS data and is of the order of ∼200 K (Goguen et al., 2013), thus much warmer than the temperatures reported here. However, since the static temperature of the mixture varies very rapidly within approximately one vent diameter of the surface in a gas-dynamic expansion into vacuum, the values we find close to the triple point but below the Goguen et al. (2013) sidewall temperature appear reasonable.

We derive an ice grain single radius of 1.1 ± 0.46 μm for one vent during INMS E14. Mahieux et al. (2019) computed the plumes using DSMC and assumed that the outgassed material is composed of water vapor and one single particle size ice grain population. As discussed in Section 2.1, this approximation will likely have minimal impact on the DSMC flow computations since the flow material expands within the collisional regime near the vent, where the particle size distribution influences momentum and energy transfer during collisions.

The ice grain radius influences the flow in terms of the number of collisions, and thus momentum and energy transfer between water vapor molecules and ice grains at a constant mass flow rate and ice grain mass percentage. Because grain mass scales with the particle size cubed, at constant mass flow rate and ice grain mass percentage, larger ice grain radii imply a lower ice grain number density. This affects the collision rate between the water vapor molecules and grains in the first few meters of flow above the surface. Ice grain radii have been measured by the VIMS, ISS, and CDA instruments (see Postberg, Clerk, et al. (2018) and references therein). The CAPS instrument also reported much smaller grains, on the order of a few nm (Dong et al., 2015), probably resulting from the condensation of the water vapor during the expansion and cooling process. While the effect of grain condensation/sublimation was not considered in this work, it was studied by Yeoh et al. (2015). The CDA instrument measured grain size distributions that were consistent with imaging. The observed correlation between grain size and grain speed makes the plume stratified by grain size, that is, larger grains are ejected moving slower and hence rise ballistically only to lower altitudes versus smaller and faster moving grains (Ershova et al., 2024; Postberg et al., 2011). Hedman et al. (2009) derived the ice particle speed dependence on altitude from VIMS observations, which roughly agrees with the plume dynamics paper by Schmidt et al. (2008).

21699100, 2025, 9, Downloaded from https://agupubs.onlinelibrary.wiley.com/doi/10.1029/2025JE009008 by Dtsch Zentrum F. Luft-U. Raum Fahrt In D. Helmholtz Gemein., Wiley Online Library on [18/08/2026]. See the Terms and Conditions (https://onlinelibrary.wiley.com/terms-and-conditions) on Wiley Online Library for rules of use; OA articles are governed by the applicable Creative Commons License

Finally, we note that introducing a full-size distribution would add several poorly constrained parameters (e.g., modal radius, width, multi-population fractions), which in an already under-constrained inverse problem would reduce numerical stability without delivering additional observables to calibrate those extra degrees of freedom.

Finally, we could increase the constraints on the longitude, latitude, azimuth and zenith angles of several vents based on the values reported by Porco et al. (2014). We acknowledge that this improvement is probably of lesser interest as the vents' position and orientation probably vary with time (Souček et al., 2024; Teolis et al., 2017).

We note that the fact that only the longitude of vent 45 is retrieved, while its latitude remains unconstrained, reflecting the projection of surface displacements onto Cassini's observation geometry. During the relevant flyby, shifting the vent east–west (i.e., in longitude) causes the plume cone to intersect the UVIS sampling path more or less directly, producing a measurable change in the observed water-vapor profile. By contrast, shifting the vent north–south (i.e., in latitude) moves the plume along the direction of spacecraft motion, which alters the timing but not the amplitude of the density signature and thus yields little change in the correlation coefficient. This coordinate-dependent effect is a general feature of our sensitivity maps: only those displacements whose projection onto the instrument's line of sight significantly modulate the sampled density can be robustly constrained.

5. Conclusions

We propose a computationally efficient and robust method to expand the number density field of a single geyser venting a mixture of water vapor and water-ice grains at supersonic speed at the vent. The number density, velocity, and kinetic and rotational temperature at an altitude of 10 km above the moon's surface are obtained from a parametric study presented by Mahieux et al. (2019), which allows one to consider variations of the mass flow, radius of the vent, initial speed of the water vapor, initial speed of the water-ice grains, mass ratio between the two phases of water, spreading angle, initial temperature, and diameter of the ice grains. The study by Mahieux et al. (2019) is based on comprehensive and computationally expensive DSMC calculations of the geyser fields considering collisions between water vapor molecules and single particle size water-ice grains up to 10 km altitude. In that study, water vapor and water ice particles are treated as two separate species. Thus, the physical model includes more physics than earlier simpler models and utilizes DSMC and other modeling to represent that physics correctly. In the present work, the plumes are expanded to higher altitudes using a quasi-analytical method, which considers the external forces experienced by the geyser and performs the calculation very rapidly (<1 s using one CPU).

We use this method to calculate the sensitivity of the INMS and UVIS Cassini instruments to the vent parameters listed above, considering the location and orientation of the 98 vents reported by Porco et al. (2014), these four geographical parameters (latitude and longitude, azimuth and zenith relative angles) are also considered free parameters.

We consider six INMS observations and local water vapor number density results and show that we obtain correlations to the mass flow of many vents. Following the same approach, we consider the UVIS solar occultation observation geometry and obtain a positive correlation to the mass flow of nearly all vents. But only a few vents have other parameters that are correlated.

Next, we apply the sensitivity study to compute and present least-squares fits of the INMS E3, E5, E7, E14, E17, and E18 and the UVIS solar occultation water vapor number density observations of the Enceladus geysers. A physically suitable model introduces many possible parameters to fit. The fits we present herein consider the sensitivity study used to reduce the problem's parametric dimensionality based on the observation geometry.

The fits were performed using a specific least-squares Levenberg-Marquardt algorithm that determines the number of free vent parameters that can be inferred reliably. The total mass flow rates in the entire Enceladus plume are smaller than those found in the literature for the INMS observations and equivalent for the UVIS solar occultation. We believe these differences arise because this work uses accurate analytical expressions for the flow fields at high altitudes derived from detailed, sophisticated DSMC computations (Mahieux et al., 2019) unlike prior work that used simple collisionless flow. The mixture exit temperature could be constrained for two sources using the UVIS solar occultation with values of 60.8 ± 15.7 K and 44.5 ± 11 K, close to the water triple point. The ice grain radius was constrained for one source with a 1.1 ± 0.46 μm value. Variations in the reported longitude, azimuth, and zenith angles of the jet's pointing directions were also tentatively fitted and showed improvement from the values reported by Porco et al. (2014).

21699100, 2025, 9, Downloaded from https://agupubs.onlinelibrary.wiley.com/doi/10.1029/2025JE009008 by Dtsch Zentrum F. Luft-U. Raum Fahrt In D. Helmholtz Gemein., Wiley Online Library on [18/08/2026]. See the Terms and Conditions (https://onlinelibrary.wiley.com/terms-and-conditions) on Wiley Online Library for rules of use; OA articles are governed by the applicable Creative Commons License

The procedure described here can significantly decrease the number of free parameters used in the vent parameter fitting procedure. Considering the list of parameters to which each measurement geometry is sensitive is thus a time-saving and reliable way to reduce the size of the problem to be solved. Moreover, the same process can be used for future mission planning of instrument use during similar operations to extract the maximum information from flybys. Indeed, the method presented in this work only considers the geometry of the observation and the physics incorporated in the models of the flows, not the actual measured data. It should be noted that the list of remote and in situ observations considered is not exhaustive. Other classes of observations, for example, VIMS, CDA, and ISS, might display different sensitivities and assist in constraining plume parameters. A similar sensitivity study can be applied to these other types of observations to guide attempts to retrieve plume characteristics.

Data Availability Statement

This section aims to comply with the availability requirements for data and software tools.

The INMS and UVIS CASSINI data used in this work are available on the NASA Planetary Data System at https://pds-atmospheres.nmsu.edu/data_and_services/atmospheres_data/Cassini/Cassini.html.

The code used to determine the sensitive parameters using the Pearson coefficients is available in MATLAB. The results are plotted and tabulated in Appendix C in Supporting Information S1, Section 3, and both tables and figures are available to download (Mahieux, 2025).

The Levenberg-Marquardt routine used for the fits is available at https://www.mathworks.com/matlabcentral/fileexchange/53449-levenberg-marquardt-toolbox.

The final results from the fits, for each set of fitted variables for each instrument, are available at the permanent repository hosted at The University of Texas at Austin (Mahieux, 2025). They contain zip files of all the results from the least-squares fits in MATLAB files (.mat).

Acknowledgments

NASA Cassini Data Analysis Program (CDAP) grant NNXI6AI52G supported AM, DG, PV, and LT research. The Texas Advanced Computing Center (TACC) partially provided computational resources. JHW received funding via a consulting contract with Southwest Research Institute from NASA Grant 80NSSC21K016.

References

Burger, M. H., Sittler, E. C., Johnson, R. E., Smith, H. T., Tucker, O. J., & Shematovich, V. I. (2007). Understanding the escape of water from Enceladus. *Journal of Geophysical Research*, *112*(A6), A06219. https://doi.org/10.1029/2006ja012086

Dayton-Oxland, R., Huybrighs, H. L. F., Winterhalder, T. O., Mahieux, A., & Goldstein, D. (2023). In-situ detection of Europa's water plumes is harder than previously thought. *Icarus*, *395*, 115488. https://doi.org/10.1016/j.icarus.2023.115488

Dentler, A. (2024). Levenberg-Marquardt toolbox. *MATLAB Central File Exchange*.

Dong, Y., Hill, T. W., Teolis, B. D., Magee, B. A., & Waite, J. H. (2011). The water vapor plumes of Enceladus. *Journal of Geophysical Research*, *116*(A10), A10204. https://doi.org/10.1029/2011ja016693

Dong, Y., Hill, T. W., & Ye, S.-Y. (2015). Characteristics of ice grains in the Enceladus plume from Cassini observations. *Journal of Geophysical Research: Space Physics*, *120*(2), 915–937. https://doi.org/10.1002/2014ja020288

Ershova, A., Schmidt, J., Postberg, F., Khawaja, N., Nölle, L., Srama, R., et al. (2024). Modeling the Enceladus dust plume based on in situ measurements performed with the cassini cosmic dust analyzer. *Astronomy & Astrophysics*, *689*, A114. https://doi.org/10.1051/0004-6361/202450429

Goguen, J. D., Buratti, B. J., Brown, R. H., Clark, R. N., Nicholson, P. D., Hedman, M. M., et al. (2013). The temperature and width of an active fissure on Enceladus measured with Cassini VIMS during the 14 April 2012 south pole flyover. *Icarus*, *226*(1), 1128–1137. https://doi.org/10.1016/j.icarus.2013.07.012

Goldstein, D. B., Hedman, M., Manga, M., Perry, M., & Spitale, J. B. T. (2018). Enceladus plume dynamics: From surface to space. In U. O. Arizona (Ed.), *Enceladus and the icy moons of Saturn* (pp. 175–194).

Hansen, C. J., Esposito, L., Colwell, J., Hendrix, A., Portyankina, G., Stewart, A., & West, R. (2020). The composition and structure of enceladus' plume from the complete set of cassini UVIS occultation observations. *Icarus*, *344*, 113461. https://doi.org/10.1016/j.icarus.2019.113461

Hansen, C. J., Esposito, L., Stewart, A. I. F., Colwell, J., Hendrix, A., Pryor, W., et al. (2006). Enceladus' water vapor plume. *Science.*, *311*(5766), 1422–1425. https://doi.org/10.1126/science.1121254

Hansen, C. J., Esposito, L. W., Stewart, A. I. F., Meinke, B., Wallis, B., Colwell, J. E., et al. (2008). Water vapour jets inside the plume of gas leaving Enceladus. *Nature*, *456*(7221), 477–479. https://doi.org/10.1038/nature07542

Hansen, C. J., Shemansky, D. E., Esposito, L. W., Stewart, A. I. F., Lewis, B. R., Colwell, J. E., et al. (2011). The composition and structure of the Enceladus plume. *Geophysical Research Letters*, *38*(11), L11202. https://doi.org/10.1029/2011gl047415

Hedman, M. M., Gosmeyer, C. M., Nicholson, P. D., Sotin, C., Brown, R. H., Clark, R. N., et al. (2013). An observed correlation between plume activity and tidal stresses on Enceladus. *Nature*, *500*(7461), 182–184. https://doi.org/10.1038/nature12371

Hedman, M. M., Nicholson, P. D., Showalter, M. R., Brown, R. H., Buratti, B. J., & Clark, R. N. (2009). Spectral observations of the Enceladus plume with Cassini-VIMS. *The Astrophysical Journal*, *693*(2), 1749–1762. https://doi.org/10.1088/0004-637x/693/2/1749

Higdon, K. J., Goldstein, D. B., & Varghese, P. L. (2017). Sensitivity analysis of direct simulation Monte carlo parameters for ionizing hypersonic flows. *Journal of Thermophysics and Heat Transfer*, *32*(1), 90–102. https://doi.org/10.2514/1.t5094

Howett, C. J. A., Spencer, J. R., Pearl, J., & Segura, M. (2011). High heat flow from Enceladus' south polar region measured using 10–600 cm$−1 $ Cassini/CIRS data. *Journal of Geophysical Research*, *116*(E3), E03003. https://doi.org/10.1029/2010je003718

21699100, 2025, 9, Downloaded from https://agupubs.onlinelibrary.wiley.com/doi/10.1029/2025JE009008 by Dtsch Zentrum F. Luft-U. Raum Fahrt In D. Helmholtz Gemein., Wiley Online Library on [18/08/2026]. See the Terms and Conditions (https://onlinelibrary.wiley.com/terms-and-conditions) on Wiley Online Library for rules of use; OA articles are governed by the applicable Creative Commons License

Ingersoll, A. P., & Ewald, S. P. (2017). Decadal timescale variability of the Enceladus plumes inferred from Cassini images. *Icarus*, *282*, 260–275. https://doi.org/10.1016/j.icarus.2016.09.018

Ingersoll, A. P., & Nakajima, M. (2016). Controlled boiling on Enceladus. 2. Model of the liquid-filled cracks. *Icarus*, *272*, 319–326. https://doi.org/10.1016/j.icarus.2015.12.040

Ingersoll, A. P., & Pankine, A. A. (2010). Subsurface heat transfer on Enceladus: Conditions under which melting occurs. *Icarus*, *206*(2), 594–607. https://doi.org/10.1016/j.icarus.2009.09.015

Kempf, S., Beckmann, U., Moragas-Klostermeyer, G., Postberg, F., Srama, R., Economou, T., et al. (2008). The E ring in the vicinity of Enceladus: I. Spatial distribution and properties of the ring particles. *Icarus*, *193*(2), 420–437. https://doi.org/10.1016/j.icarus.2007.06.027

Kempf, S., Beckmann, U., & Schmidt, J. (2010). How the Enceladus dust plume feeds Saturn's E ring. *Icarus*, *206*(2), 446–457. https://doi.org/10.1016/j.icarus.2009.09.016

Khawaja, N., Postberg, F., Hillier, J., Klenner, F., Kempf, S., Nölle, L., et al. (2019). Low-mass nitrogen-oxygen-bearing, and aromatic compounds in Enceladean ice grains. *Monthly Notices of the Royal Astronomical Society*, *489*(4), 5231–5243. https://doi.org/10.1093/mnras/stz2280

Kieffer, S. W., Lu, X., Bethke, C. M., Spencer, J. R., Marshak, S., & Navrotsky, A. (2006). A clathrate reservoir hypothesis for enceladus' south polar plume. *Science*, *314*(5806), 1764–1766. https://doi.org/10.1126/science.1133519

Kite, E. S., & Rubin, A. M. (2016). Sustained eruptions on Enceladus explained by turbulent dissipation in tiger stripes. *PNAS*, *113*(15), 3972–3975. https://doi.org/10.1073/pnas.1520507113

Magee, B. A., & Waite, J. H. (2017). Neutral gas composition of enceladus' plume–Model parameter insights from Cassini-INMS. In *Lunar and Planetary Science Conference*.

Mahieux, A. (2025). *Enceladus water plume modeling using DSMC*. Texas Data Repository. https://doi.org/10.18738/T8/IXCUXK

Mahieux, A., Goldstein, D. B., Varghese, P., & Trafton, L. (2019). Parametric study of water vapor and water ice particles plumes based on DSMC calculations: Application to the Enceladus geysers. *Icarus*, *319*, 729–744. https://doi.org/10.1016/j.icarus.2018.10.022

Matson, D. L., Davies, A. G., Johnson, T. V., Combe, J. P., McCord, T. B., Radebaugh, J., & Singh, S. (2018). Enceladus' near-surface CO2 gas pockets and surface frost deposits. *Icarus*, *302*, 18–26. https://doi.org/10.1016/j.icarus.2017.10.025

McDoniel, W. J., Goldstein, D. B., Varghese, P. L., & Trafton, L. M. (2015). Three-dimensional simulation of gas and dust in Io's Pele plume. *Icarus*, *257*, 251–274. https://doi.org/10.1016/j.icarus.2015.03.019

Nakajima, M., & Ingersoll, A. P. (2016). Controlled boiling on Enceladus. 1. Model of the vapor-driven jets. *Icarus*, *272*, 309–318. https://doi.org/10.1016/j.icarus.2016.02.027

Nimmo, F., Porco, C., & Mitchell, C. (2014). Tidally modulated eruptions on Enceladus: Cassini ISS observations and models. *The Astronomical Journal*, *148*(3), 46. https://doi.org/10.1088/0004-6256/148/3/46

Perry, M. E., Teolis, B., Hurley, D., Magee, B., Waite, J., Brockwell, T., et al. (2015). Cassini INMS measurements of Enceladus plume density. *Icarus*, *257*, 139–162. https://doi.org/10.1016/j.icarus.2015.04.037

Porco, C., Nino, D. D., & Nimmo, F. (2014). How the geysers, tidal stresses, and thermal emission across the south polar terrain of Enceladus are related. *The Astronomical Journal*, *148*(3), 45. https://doi.org/10.1088/0004-6256/148/3/45

Porco, C. C., Helfenstein, P., Thomas, P. C., Ingersoll, A. P., Wisdom, J., West, R., et al. (2006). Cassini observes the active south pole of Enceladus. *Science*, *311*(5766), 1393–1401. https://doi.org/10.1126/science.1123013

Portyankina, G., Esposito, L., Hansen, C., & Villanueva, G. (2018). *Search for variability between Enceladus jets erupting from different tiger stripes with UVIS*. DPS Meeting.

Portyankina, G., Esposito, L. W., Ali, A., & Hansen, C. J. (2016). Modeling of the Enceladus water vapor jets for interpreting UVIS star and solar occultation observations. *Lunar and Planetary Science Conference*.

Portyankina, G., Esposito, L. W., Aye, K.-M., Hansen, C. J., & Ali, A. (2022). Modeling the complete set of Cassini's UVIS occultation observations of Enceladus plume. *Icarus*, *383*, 114918. https://doi.org/10.1016/j.icarus.2022.114918

Postberg, F., Clark, R. N., Hansen, C. J., Coates, A. J., Dalle Ore, C. M., Scipioni, F., et al. (2018a). Plume and surface composition of Enceladus. In U. O. Arizona (Ed.), *Enceladus and the icy moons of Saturn* (pp. 129–162).

Postberg, F., Kempf, S., Schmidt, J., Brilliantov, N., Beinsen, A., Abel, B., et al. (2009). Sodium salts in E-ring ice grains from an ocean below the surface of Enceladus. *Nature*, *459*(7250), 1098–1101. https://doi.org/10.1038/nature08046

Postberg, F., Khawaja, N., Abel, B., Choblet, G., Glein, C. R., Gudipati, M. S., et al. (2018). Macromolecular organic compounds from the depths of Enceladus. *Nature*, *558*(7711), 564–568. https://doi.org/10.1038/s41586-018-0246-4

Postberg, F., Schmidt, J., Hillier, J., Kempf, S., & Srama, R. (2011). A salt-water reservoir as the source of a compositionally stratified plume on Enceladus. *Nature*, *474*(7353), 620–622. https://doi.org/10.1038/nature10175

Saur, J., Schilling, N., Neubauer, F. M., Strobel, D. F., Simon, S., Dougherty, M. K., et al. (2008). Evidence for temporal variability of Enceladus' gas jets: Modeling of Cassini observations. *Journal of Geophysical Research*, *35*(20), L20105. https://doi.org/10.1029/2008gl035811

Schenk, P. M., Clark, R. N., Howett, C. J. A., Verbiscer, A. J., & Waite, J. H. (2018). *Enceladus and the icy moons of Saturn*. University of Arizona Press.

Schmidt, J., Brilliantov, N., Spahn, F., & Kempf, S. (2008). Slow dust in Enceladus; plume from condensation and wall collisions in tiger stripe fractures. *Nature*, *451*(7179), 685–688. https://doi.org/10.1038/nature06491

Science Special Issue. (2006). Cassini at enceladus. *Science*, *311*.

Smith, H. T., Johnson, R. E., Perry, M. E., Mitchell, D. G., McNutt, R. L., & Young, D. T. (2010). Enceladus plume variability and the neutral gas densities in saturn's magnetosphere. *Journal of Geophysical Research*, *115*(A10), A10252. https://doi.org/10.1029/2009ja015184

Souček, O., Běhounková, M., Lanzendörfer, M., Tobie, G., & Choblet, G. (2024). Variations in plume activity reveal the dynamics of water-filled faults on Enceladus. *Nature Communications*, *15*(1), 7405. https://doi.org/10.1038/s41467-024-51677-z

Spencer, J. R., Pearl, J. C., Segura, M., Flasar, F. M., Mamoutkine, A., Romani, P., et al. (2006). Cassini encounters Enceladus: Background and the discovery of a south polar hot spot. *Science*, *311*(5766), 1401–1405. https://doi.org/10.1126/science.1121661

Spitale, J. N., Hurford, T. A., Rhoden, A. R., Berkson, E. E., & Platts, S. S. (2015). Curtain eruptions from Enceladus' south-polar terrain. *Nature*, *521*(7550), 57–60. https://doi.org/10.1038/nature14368

Tenishev, V., Combi, M. R., Teolis, B. D., & Waite, J. H. (2010). An approach to numerical simulation of the gas distribution in the atmosphere of Enceladus. *Journal of Geophysical Research*, *115*(A9), A09302. https://doi.org/10.1029/2009ja015223

Tenishev, V., Öztürk, D. C. S., Combi, M. R., Rubin, M., Waite, J. H., & Perry, M. (2014). Effect of the tiger stripes on the water vapor distribution in Enceladus' exosphere. *Journal of Geophysical Research: Planets*, *119*, 2658–2667. https://doi.org/10.1002/2014JE004700

Tenishev, V., Shou, Y., Lee, Y., Ma, Y., & Combi, M. R. (2024). Modeling exospheres: Analytical and numerical methods with application examples. *Frontiers in Astronomy and Space Sciences*, *11*, 1484360. https://doi.org/10.3389/fspas.2024.1484360

21699100, 2025, 9, Downloaded from https://agupubs.onlinelibrary.wiley.com/doi/10.1029/2025JE009008 by Dtsch Zentrum F. Luft-U. Raum Fahrt In D. Helmholtz Gemein., Wiley Online Library on [18/08/2026]. See the Terms and Conditions (https://onlinelibrary.wiley.com/terms-and-conditions) on Wiley Online Library for rules of use; OA articles are governed by the applicable Creative Commons License

Teolis, B. D., Perry, M. E., Hansen, C. J., Waite, J. H., Porco, C. C., Spencer, J. R., & Howett, C. J. A. (2017). Enceladus plume structure and time variability: Comparison of cassini observations. *Astrobiology*, *17*(9), 926–940. https://doi.org/10.1089/ast.2017.1647

Tian, F., Stewart, A. I. F., Toon, O. B., Larsen, K. W., & Esposito, L. W. (2007). Monte Carlo simulations of the water vapor plumes on Enceladus. *Icarus*, *188*(1), 154–161. https://doi.org/10.1016/j.icarus.2006.11.010

Tucker, O. J., Combi, M. R., & Tenishev, V. M. (2015). 2D models of gas flow and ice grain acceleration in Enceladus' vents using DSMC methods. *Icarus*, *257*, 362–376. https://doi.org/10.1016/j.icarus.2015.05.012

Waite, J. H., Combi, M. R., Ip, W. H., Cravens, T. E., McNutt, R. L., Jr., Kasprzak, W., et al. (2006). Cassini ion and neutral mass spectrometer: Enceladus plume composition and structure. *Science*, *311*(5766), 1419–1422. https://doi.org/10.1126/science.1121290

Waite, J. H., Glein, C. R., Perryman, R. S., Teolis, B. D., Magee, B. A., Miller, G., et al. (2017). Cassini finds molecular hydrogen in the Enceladus plume: Evidence for hydrothermal processes. *Science*, *356*(6334), 155–159. https://doi.org/10.1126/science.aai8703

Yeoh, S. K., Chapman, T. A., Goldstein, D. B., Varghese, P. L., & Trafton, L. M. (2015). On understanding the physics of the Enceladus south polar plume via numerical simulation. *Icarus*, *253*, 205–222. https://doi.org/10.1016/j.icarus.2015.02.020

Yeoh, S. K., Li, Z., Goldstein, D. B., Varghese, P. L., Levin, D. A., & Trafton, L. M. (2017). Constraining the Enceladus plume using numerical simulation and Cassini data. *Icarus*, *281*, 357–378. https://doi.org/10.1016/j.icarus.2016.08.028

Zaharias, M. C., Mahieux, A., Goldstein, D. B., Varghese, P. V., & Trafton, L. M. (2023). Simulation of H{_2} in the Conduits of Enceladus [#2688]. *Lunar and Planetary Science Conference*.

21699100, 2025, 9, Downloaded from https://agupubs.onlinelibrary.wiley.com/doi/10.1029/2025JE009008 by Dtsch Zentrum F. Luft-U. Raum Fahrt In D. Helmholtz Gemein., Wiley Online Library on [18/08/2026]. See the Terms and Conditions (https://onlinelibrary.wiley.com/terms-and-conditions) on Wiley Online Library for rules of use; OA articles are governed by the applicable Creative Commons License